



OPEN

SUBJECT AREAS:

SENSORS AND  
BIOSENSORS

SENSORS

Received  
29 November 2013Accepted  
20 January 2014Published  
17 February 2014Correspondence and  
requests for materials  
should be addressed to  
G.U.K. (kulkarni@  
jncasr.ac.in)\* These authors  
contributed equally to  
this work.

# Ultrafast response humidity sensor using supramolecular nanofibre and its application in monitoring breath humidity and flow

Umesha Mogera<sup>1\*</sup>, Abhay A. Sagade<sup>1\*</sup>, Subi J. George<sup>2</sup> & Giridhar U. Kulkarni<sup>1</sup>

<sup>1</sup>Chemistry and Physics of Materials Unit and Thematic Unit on Nanochemistry, Jawaharlal Nehru Centre for Advanced Scientific Research, Jakkur P.O., Bangalore 560064, India, <sup>2</sup>Supramolecular Chemistry Laboratory, New Chemistry Unit, Jawaharlal Nehru Centre for Advanced Scientific Research, Jakkur P.O., Bangalore 560064, India.

Measuring humidity in dynamic situations calls for highly sensitive fast response sensors. Here we report, a humidity sensor fabricated using solution processed supramolecular nanofibres as active resistive sensing material. The nanofibres are built via self-assembly of donor and acceptor molecules (coronene tetracarboxylate and dodecyl methyl viologen respectively) involved in charge transfer interactions. The conductivity of the nanofibre varied sensitively over a wide range of relative humidity (RH) with unprecedented fast response and recovery times. Based on UV-vis, XRD and AFM measurements, it is found that the stacking distance in the nanofibre decreases slightly while the charge transfer band intensity increases, all observations implying enhanced charge transfer interaction and hence the conductivity. It is demonstrated to be as a novel breath sensor which can monitor the respiration rate. Using two humidity sensors, a breath flow sensor was made which could simultaneously measure RH and flow rate of exhaled nasal breath. The integrated device was used for monitoring RH in the exhaled breath from volunteers undergoing exercise and alcohol induced dehydration.

Humidity sensing is important in different settings, in chemical industry, hospitals, agricultural fields and so on<sup>1,2</sup>. A sensor working with fast response and recovery (typically fraction of a second) finds niche applications in situations where the humidity value may change dynamically. Such application areas include industrial process controls, meteorology and various medical diagnostics including monitoring human exhaled breath<sup>3-7</sup>. This explains the need of low cost humidity sensors with ultra-fast response, high sensitivity and stability. Although the literature is abound with humidity sensors<sup>8</sup>, those with fast response form only a small subset (see Supplementary Table S1). The subset includes those based on inorganic materials in the form of nanowires<sup>9</sup>, nanotubes<sup>10,11</sup>, thin films of oxides<sup>12-14</sup> and of few sulfides<sup>15,16</sup> as well. Similarly, there are examples from organic and composite materials, a notable one being nafion persulphonate<sup>4</sup> with tens of milliseconds of response time. Very recently, Borini et al.<sup>17</sup> have reported response time of 30 ms for a graphene oxide based sensor. In addition to this, there are advancements in fabrication of humidity sensors using optic fibre based sensor technology<sup>18,19</sup>. There have been reports of humidity sensors using hybrid microcavity<sup>20</sup>, AFM micro-cantilevers<sup>21</sup>, plasmonic materials<sup>22</sup> etc. Fabrication of flexible, printable, chipless and wireless humidity sensors and integrating them with CMOS technology has been recently reported intended for various humidity related applications<sup>23-25</sup>. The basic mechanism of humidity detection in the above materials is based on the change in proton/ionic conduction (resistive), dielectric constant (capacitive), refractive index (optical), frequency (impedance) or in mass, of the active material with the humidity level<sup>26</sup>. Organic humidity sensors are particularly attractive since the sensing material can be prepared by simple solution processes unlike in inorganic sensors which demand expensive preparation techniques such as chemical vapor deposition, vapour-liquid-solid growth etc.; however, organic sensors usually lack stability in terms of device performance<sup>27-29</sup>.

Supramolecular systems are relatively a new class of organic materials, built via non-covalent interactions among the molecular ingredients<sup>30</sup>. Fabricating functional devices such as FETs, solar cells, sensors from controlled organization of supramolecular components is considered as a promising area of research<sup>31-34</sup>. It takes the advantage of intermediate size regime, few tens of nm to  $\mu\text{m}$ , when compared to single molecule (few nm) and

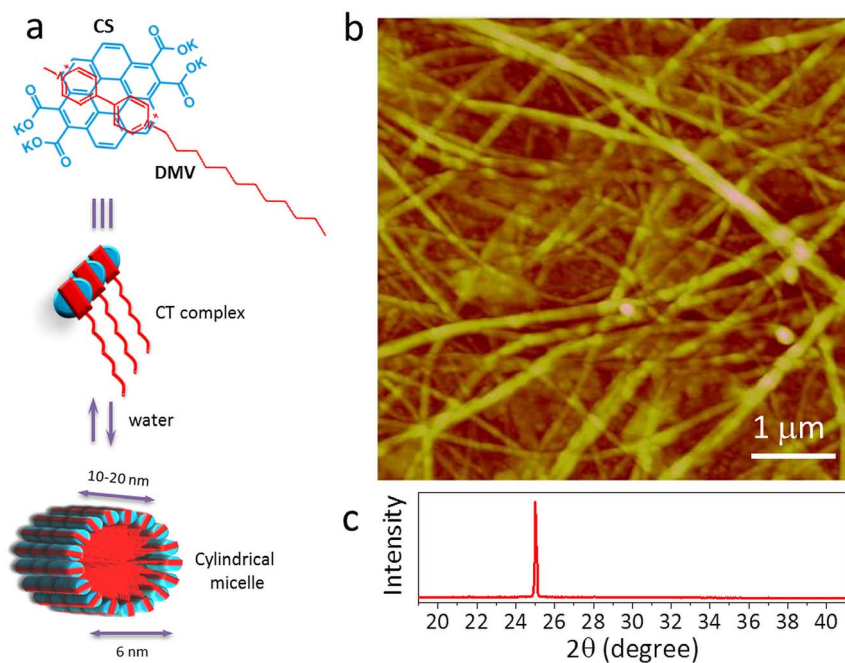


**Figure 1 | Structural aspects of CS-DMV nanofibres.** (a) Molecular structure and schematic of the CT complex involving co-facial arrangement of the aromatic donor, coronene tetracarboxylate (CS) and the acceptor, dodecyl methyl viologen derivative (DMV) (top). The stacking of the complex units to form a cylindrical micelle in presence of water, is depicted. (b) Tapping mode AFM image of a nanofibre carpet film. The z scale in the image is 20 nm. (c) XRD pattern of the film measured in ambient conditions (26°C, 35% RH). The peak at  $2\theta \approx 25.031^\circ$  corresponds to  $d$ -spacing of 3.5545 Å rising from the  $\pi$ - $\pi$  stacking in nanofibres.

polymer films ( $\approx \mu\text{m}$ )<sup>35,36</sup>. Recently, Herzer et al.<sup>37</sup> reported change in color of supramolecular polymer films upon exposure to humidity. Among various supramolecular systems, 1-D nanowires are of particularly interesting since they provide low scattering conducting paths<sup>38–40</sup> and easy alignment across the electrodes<sup>41</sup>. We have recently embarked on a supramolecular one-dimensional (1-D) system, a charge transfer donor and acceptor couple grown in the form of nanofibre, to use as an active channel material in field-effect transistor which worked in the ambient conditions and showed high hole mobility and carrier concentration<sup>42</sup>. During the measurements, it was observed that the device performance was sensitively dependent on the laboratory humidity conditions. In the present article, we have examined this aspect in detail and developed a humidity sensor based on resistive response of the supramolecular nanofibre at different levels of humidity. The associated structural changes and interactions therein, have been examined using UV-vis absorption, X-ray diffraction (XRD) and atomic force microscopy (AFM). The versatility of the device is demonstrated by sensing humidity very close to a water drop with high sensitivity, of relevance in touchless sensing. The response time being around 10 ms (fastest ever reported), the device could be implemented meritoriously for continuous monitoring of humidity in human breath.

## Results

**Supramolecular nanofibres.** The charge transfer (CT) nanofibres were prepared by the self-assembly of coronene-viologen based donor and acceptor (D and A) pairs in water<sup>43</sup> (see Methods). Briefly, the potassium salt of coronene tetracarboxylate (CS) and the dodecyl substituted unsymmetric viologen derivative (DMV) are used as D and A pairs which interact via ground-state CT interactions to form a hierarchical self-assembly. In water, these two components stack themselves to form cylindrical micelles (diameter,  $\approx 6$  nm) following a surfactant-like assembly (schematic in Fig. 1a). This forms bilayers of CT-amphiphiles arranged radially with the D and A molecules stacked face-to-face along the length of

the nanofibre. The tapping mode AFM topography image in Fig. 1b shows nanofibres crystallised from 1 mM solution, of varying diameters (100–300 nm) interwoven randomly to form a carpet morphology. The XRD pattern of the carpet film in Fig. 1c shows a peak at  $2\theta \approx 25.031^\circ$  corresponding to a  $d$ -spacing of 3.5545 Å. Given the constituents in the nanofibre, this value should correspond to the  $\pi$ - $\pi$  spacings in the D and A pairs along the nanofibre. The intensity and sharpness associated with the peak indicate highly ordered nature of the D and A stacking.

**RH sensing by nanofibre film.** The performance of the nanofibres as a humidity sensor is described in Fig. 2. A drop (5  $\mu\text{L}$ , 1 mM) of the CS-DMV nanofibre solution was drop coated on gold gap electrodes on glass and allowed to dry for an hour. The device was then placed inside a humidity cell (Fig. 2a) and connected to a Keithley 4200 source unit for electrical characterisation. Moisture-nitrogen mixture of varying RH was passed through the humidity cell through the inlet as shown in Fig. 2a. As the RH increased from 5% to 65% at 0.8 V bias, the current in the nanofibres increased from  $\approx 0.1$  nA to 220 nA (Fig. 2b) and showed a small decay while RH was still on, but dropped down to 0.1 nA sharply when RH switched to 5%. The response and recovery times, measured as the time taken to reach 90% of the peak value (Fig. 2c), are 2.20 and 1.05 s respectively. The sensitivity of the device, which is a direct measure of how well a device detects per unit change of RH, is defined in this case as the change in current normalized with respect to the current at 5% RH<sup>9</sup>. The sensitivity increased rapidly as RH increased to 85% to reach a value of  $\approx 45,000$  (Fig. 2d, for current values see Supplementary Fig. S1). The fabricated devices were stable over several months when stored under ambient conditions (see Supplementary Fig. S2). The effect of environment temperature (between 10°C to 50°C) on the sensor has also been studied and described in the Supplementary Fig. S3.

**Mechanism of RH sensing.** In order to gain an insight into the observed electrical changes with RH, UV-vis absorption measure-

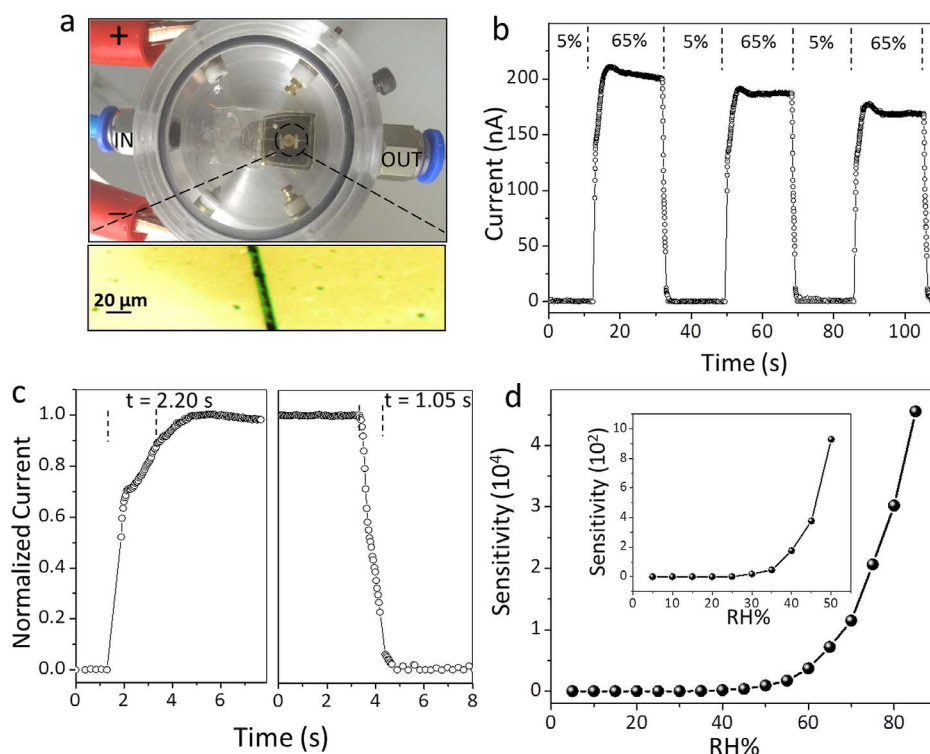


**Figure 2 | RH detection by CS-DMV nanofibre film.** (a) A photograph of the humidity detection set up used in the study. Inset is the optical microscope image of zoomed in part of the device, which consists of Au gap electrodes drop coated with 5  $\mu$ L of nanofibre suspension resulting in a nanofibre film laid across the gap. The thin film cannot be delineated due to its transparency. (b) The changes in the measured current from the film at 0.8 V as RH was switched between 5% and 65%. (c) Estimation of the response and recovery times. (d) The variation in sensitivity for different RH values for a typical device. Inset is the zoomed portion for lower RH. Line fitting is to guide the eye.

ments were carried out on a CS-DMV nanofibre carpet film as shown in Fig. 3. Few drops of the nanofibre solution were drop coated on the inner side of a quartz cuvette and allowed to evaporate. The cuvette was then closed with a rubber stopper hosting inlet and outlet for passing moisture-nitrogen mixture of varying RH. The absorption spectra of CS-DMV nanofibres film exhibit strong absorption peaks at 318 and 355 nm along with a broad band centred around 480 nm

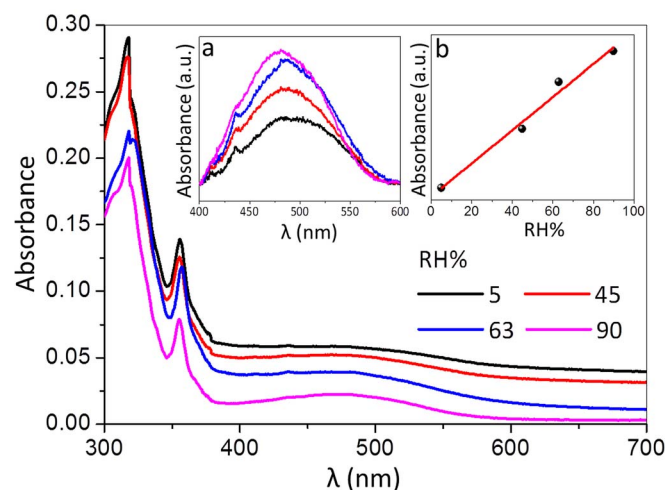


**Figure 3 | In-situ optical absorbance measurements of CS-DMV nanofibres with RH.** The change in absorbance of CS-DMV nanofibre film measured on quartz substrate from 300 to 700 nm range at different RH values. Insets are the magnified portion of the charge transfer band in the region, 400 to 600 nm, after baseline correction (a) and the plot of variation in intensity of the charge transfer band with RH (b).

which originates from the ground state intermolecular charge transfer interaction between donor and acceptor molecules<sup>43</sup>. The peak intensity is highly sensitive to any perturbation to the charge transfer interaction, which in turn influences the electrical transport through the nanofibre. The intensity of the 480 nm band does show changes with change in RH (Fig. 3), but accompanying this change, the spectral baseline also shifts due to varied transmittance of the film (*vide infra*). After baseline correction, the changes in the intensity of the 480 nm band became quite apparent (see inset (a) of Fig. 3). Indeed as shown in inset (b), the intensity was found to increase linearly with increase in RH emphasizing the role of charge transfer in electrical transport of CS-DMV nanofibre system.

Further insight into the structural changes comes from in situ X-ray diffraction measurements (Fig. 4). With increase in RH from 5% to 65%, the peak corresponding to the CS and DMV spacing ( $\pi$ - $\pi$  interaction distance) in the supramolecular assembly is found to shift from a  $2\theta$  value of  $25.027^\circ$  ( $d$ -spacing, 3.5551 Å) to  $25.040^\circ$  (3.5534 Å), the peak shift of 0.016 Å being well outside of the measurable limit ( $\pm 0.00015$  Å). The peak shift is linear (Fig. 4b) and thus follows a similar behaviour as the intensity of the charge transfer peak (Fig. 3b). Thus it appears that an increase in RH brings the CS and DMV units closer, thereby enforcing a much tighter packing in the assembly. Since the electrical transport in such systems depend sensitively on the charge transfer interaction and  $\pi$ - $\pi$  delocalization among the D and A pairs<sup>44</sup>, any small perturbation due to change in RH can bring about considerable change in conductivity.

The local changes in the nanofibre assembly as discussed above, may have some implications on the morphology of the nanofibres. AFM measurements were carried out on the nanofibre film at different RH values in an environmental hood (see Fig. 5 and Supplementary Fig. S4). At ambient humidity (42% RH), the average width of the nanofibres was  $99.6 \pm 7.6$  nm (Fig. 5a) which increased



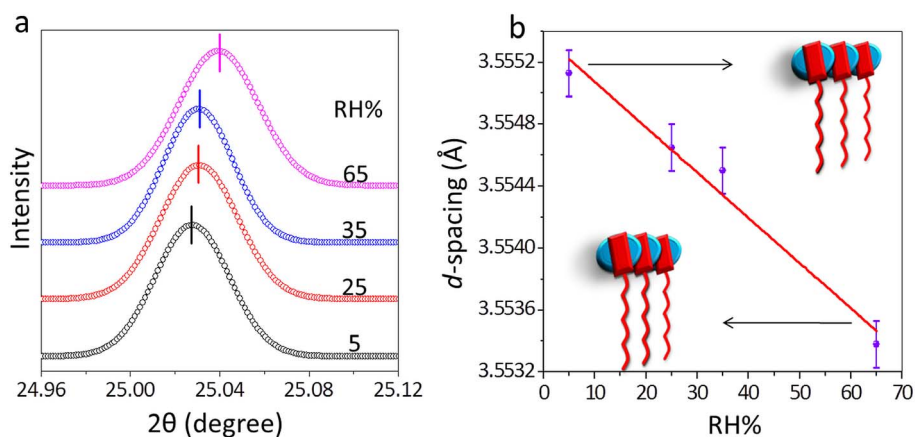


**Figure 4 | Humidity dependent XRD studies of CS-DMV nano-fibres.** (a) The XRD patterns of nanofibres film acquired at RH of 5%, 25%, 35%, and 65%. The XRD peak was recorded with step size of 0.001 degree at different RH values. The patterns are shifted vertically for clarity. The peak maxima are marked by vertical bars. (b) The variation in the XRD  $d$ -spacing with RH.

to  $118.4 \pm 9.6$  nm when the RH in the hood was changed to 15% (Fig. 5b). The concomitant change in nanofibre height was from  $6.24 \pm 1.1$  to  $5.2 \pm 1.18$  nm. As the humidity was increased to 62%, the average width decreased to  $76.4 \pm 9.0$  nm while the height increased to  $8.14 \pm 0.5$  nm (Fig. 5c). The decreasing width can enhance light transmission as seen from the downward shift of the spectral baseline in Fig. 3a. In Fig. 5d are shown the observed morphology changes with respect to a given location on a nanofibre (see arrow marks in Fig. 5a, b and c). Many such individual measurements have been performed (Supplementary Fig. S2). The observed morphology changes may be taken to indicate a tighter molecular assembly with

higher humidity around the supramolecular fibres. Under very dry conditions, the nanofibres were found to be non-conducting. Indeed, the conduction could be initiated by simply exposing to humid air.

**Determination of RH near a water drop.** As it is clear from the above observations, the CS-DMV nanofibres can be potentially used for monitoring small variations in humidity levels near a surface, for example; such ideas could be relevant in the context of next generation intelligent device components such as artificial skin or touchless screen, where the ‘sensation’ of an approaching finger or a live cell would depend on its distance from the skin<sup>15</sup>. We designed an

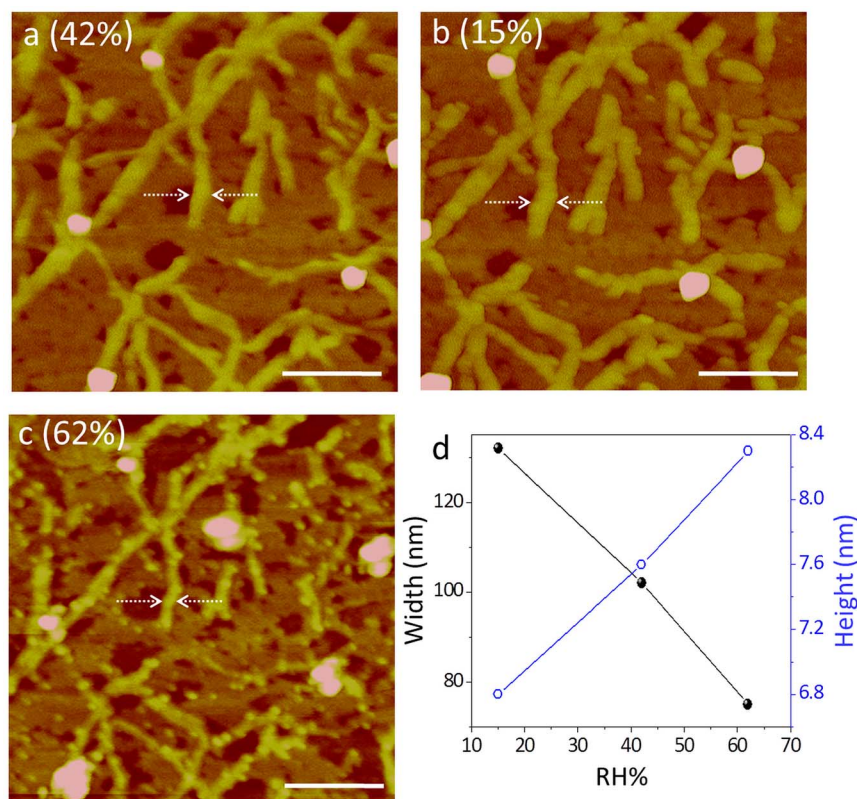


**Figure 5 | AFM analysis of nanofibres under different RH conditions.** AFM images of CS-DMV nanofibres acquired at ambient RH of 42% (a) followed by at 15% (b) and 62% (c), the last two measurements being carried out in atmospheric hood. Scale bar: 500 nm, z scale: 20 nm. (d). The variations in width (left) and height (right) of nanofibre marked in dotted lines with different RH conditions. Data from other regions are presented in the Supplementary Fig. S4.

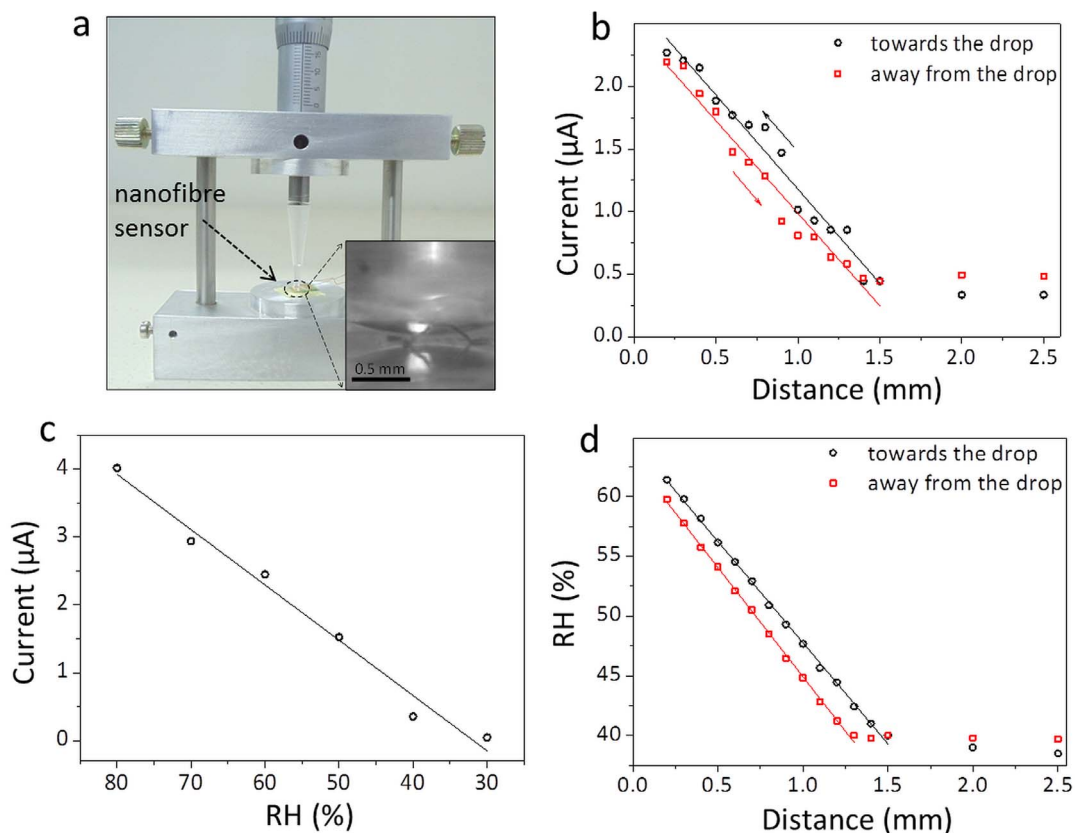


**Figure 6 | RH above a water drop.** (a) A photograph of the setup used for the study. It consists of a plastic tip carrying the tiny water drop which can be moved in vertical direction using a screw gauge arm. Inset is the magnified image when the water drop is very close to the sensor. Reflection of the drop is seen from the device surface. (b) Variation in the current (at 1 V), as the water drop is brought towards and taken away from the nanofibre sensor. (c) Variation of current through the nanofibres at different RH measured at 1 V. (d) Derived plot of variation of RH of water drop with distance.

experiment wherein the change in current through a nanofibre film was monitored while a microtip carrying a tiny water droplet made a controlled approach (see Fig. 6a), from a distance of 2.5 to 0.2 mm in steps of 0.1 mm. As seen from the plot in Fig. 6b, the current in the circuit increased from  $\approx 0.45$  to  $2.3 \mu\text{A}$  and the increase was nearly linear with distance. On retracting the tip, it followed a similar trend with slightly less current. Based on the calibration data collected for this film (Fig. 6c), we were able to estimate RH at different tip separation distances (Fig. 6d). It is interesting to see that the RH value reaches as high as 60% close to the drop and decreases gradually till 1.5 mm above which it merges with the ambient background. This trend is similar to the one reported by Feng et al.<sup>15</sup>, although this study aims at measurements much closer to the humid surface. This experiment clearly demonstrates the ‘action at a distance’ possibility in real applications with high degree of sensitivity.

**Ultrafast RH sensing using few nanofibres.** It may be noted that the nanofibre carpet device developed in this study exhibits quite fast response ( $\approx 1$ – $2$  s) comparing well with many literature examples (see Supplementary Table S1). It is known from the literature that conducting paths in carpet-like morphology come across innumerable scattering junctions, which can adversely influence the device response<sup>25–27</sup>. We have explored improving the response by fabricating a device with only few nanofibres across the gap electrodes instead of a carpet film. This was achieved by placing a  $5 \mu\text{L}$  drop of 0.1 mM CS-DMV dispersion (Fig. 7a). The change in the voltage across a standard resistor ( $20 \text{ M}\Omega$ ) as measured using an oscilloscope was quite rapid (Fig. 7b) as the humidity over the device was switched between 5% and 80% in cycles. In this case, the response

and recovery times turned out to be 8 and 24 ms respectively (Fig. 7c). To our knowledge, this is the fastest humidity sensor made so far; nafion persulphonate<sup>4</sup> and graphene oxide<sup>17</sup> based sensors come close to its performance with 30–40 ms response time (see Supplementary Table S1). The sensitivity of the device was in the range, 100–500, and its variation at different RH is shown in Supplementary Fig. S5.

**Application to human breathing order.** Motivated by the fast response and sensitivity of the sensor, we found it interesting to explore the usefulness of this device in monitoring human breath, particularly during exhale as the humidity is expected to be different (usually higher) compared to inhaled (ambient) air. Working with a healthy adult male, the variations in the RH value were monitored by holding the nanofibre device at a distance of 3.5 cm from the nose while breathing normally. Interestingly, the RH over the device showed sharp rise during exhaling and dropped to ambient value while inhaling, which was nearly repetitive corresponding to the breathing cycles (see Figure 7d). Further, the device could efficiently follow, no matter how fast or slow was the breathing (Figure 7e). In the panel given, the breathing varied from 0.3 to 5 s per cycle. Importantly, the nanofibres in the device were stable throughout.

Such a device should be of importance in breath analysis. Characterization of exhaled breath has become a simple yet powerful non-invasive method of diagnosing diseases such as asthma, cancer, diabetes etc<sup>45–50</sup>. Any serious monitoring of exhaled breath should be an online process tracking the changes in every breath cycles<sup>51,52</sup>; offline trace gas analysis suffers from inherent problems associated with sample preparation and storage, contamination, chemical transformation of the analytes, etc<sup>52</sup>. While monitoring analytes for

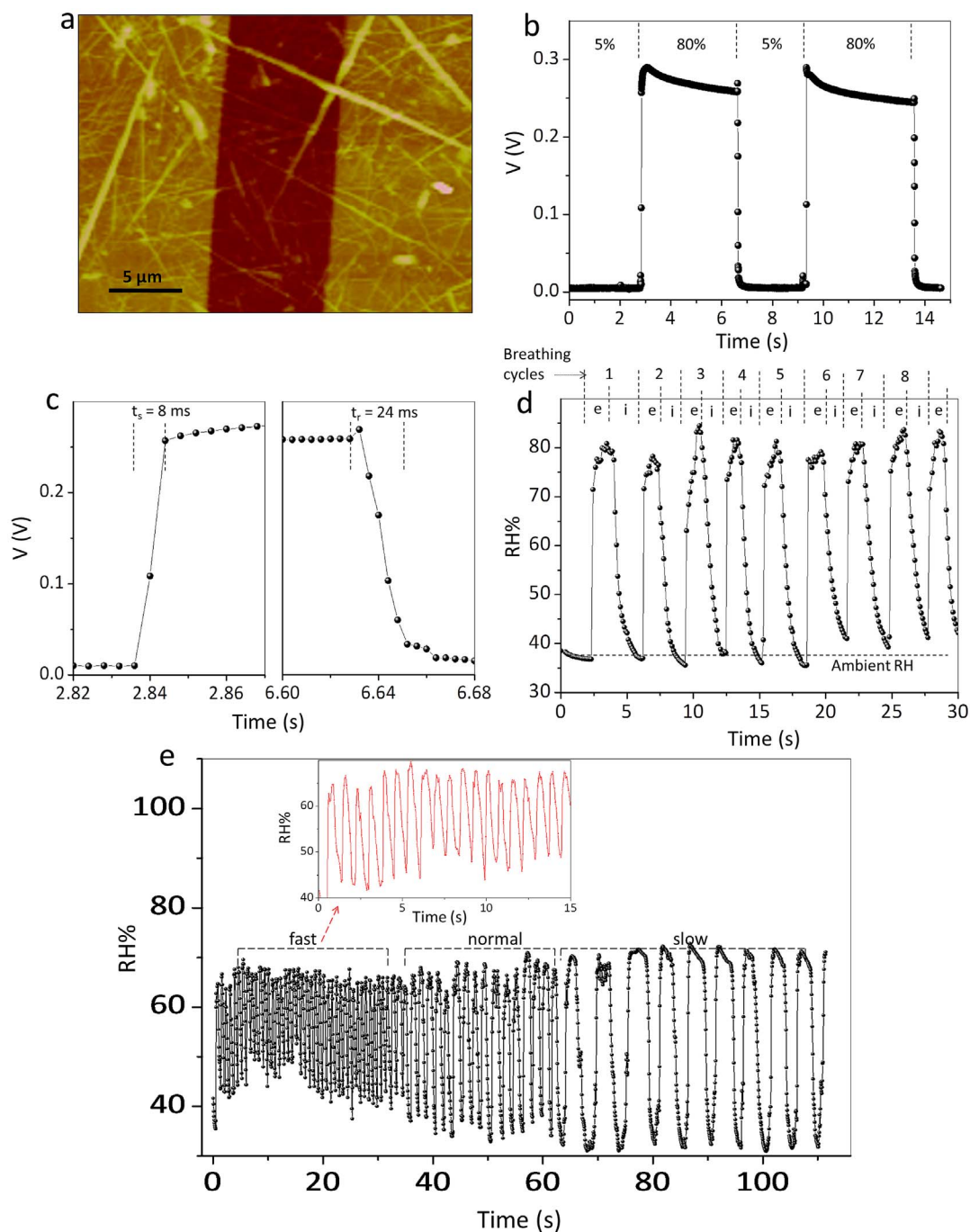


**Figure 7 | A breath RH sensor.** (a) Tapping mode AFM images of few nanofibres across gold electrodes ( $\approx 8 \mu\text{m}$ ). The z scale in the image is 20 nm. (b) The changes in output voltage measured using an oscilloscope, from a few nanofibre sensor as RH is switched between 5% and 80%. (c) Estimation of response and recovery times of the sensor. (d) Variations in the RH of the exhaled breath of a healthy person. e and i refer to the exhaling and inhaling respectively. (e) Response of the sensor at different breathing rates. Inset shows zoom in part of the response corresponding to fast breathing.

specific diseases is important, monitoring humidity itself can possibly throw some light on an individual's health such as dehydration. Although there are many indices suggested in the literature to indicate body hydration status<sup>53–55</sup>, we for the first time, have made an attempt monitor dehydration through RH in the breath.

Towards this end, we considered it important to measure simultaneously the humidity and the exhaled breath flow, the latter to increase the confidence in the measurements. We therefore, fabricated a flow cum humidity sensor using CS-DMV nanofibres (Fig. 8). The device consists of supramolecular humidity sensors, D1 and D2, placed in a glass tube 8 cm apart. The glass tube is connected to a breath receiving mask (typically used for oxygen supply to patients),

through a flow divider (see Fig. 8a); the latter was required as calibration using typical mass flow controllers proved difficult at realistic breath flow ( $\approx 10\text{--}50 \text{ kscm}^{56}$ ). As an individual breaths out into the mask, the divided flow reaches the sensor D1 at time  $t_1$  and D2 at time  $t_2$  (at half rise), and the time difference,  $\Delta t = t_2 - t_1$  (see Fig. 8b) was used for calculating the flow. The humidity could be measured from both sensors using the respective calibration curves (see Supplementary Fig. S6). By measuring both humidity and flow rate for every breath cycle, the humidity measurement could be validated.

The above setup was used in varied conditions of volunteers. We have monitored the RH present in nasal breath rather than that from



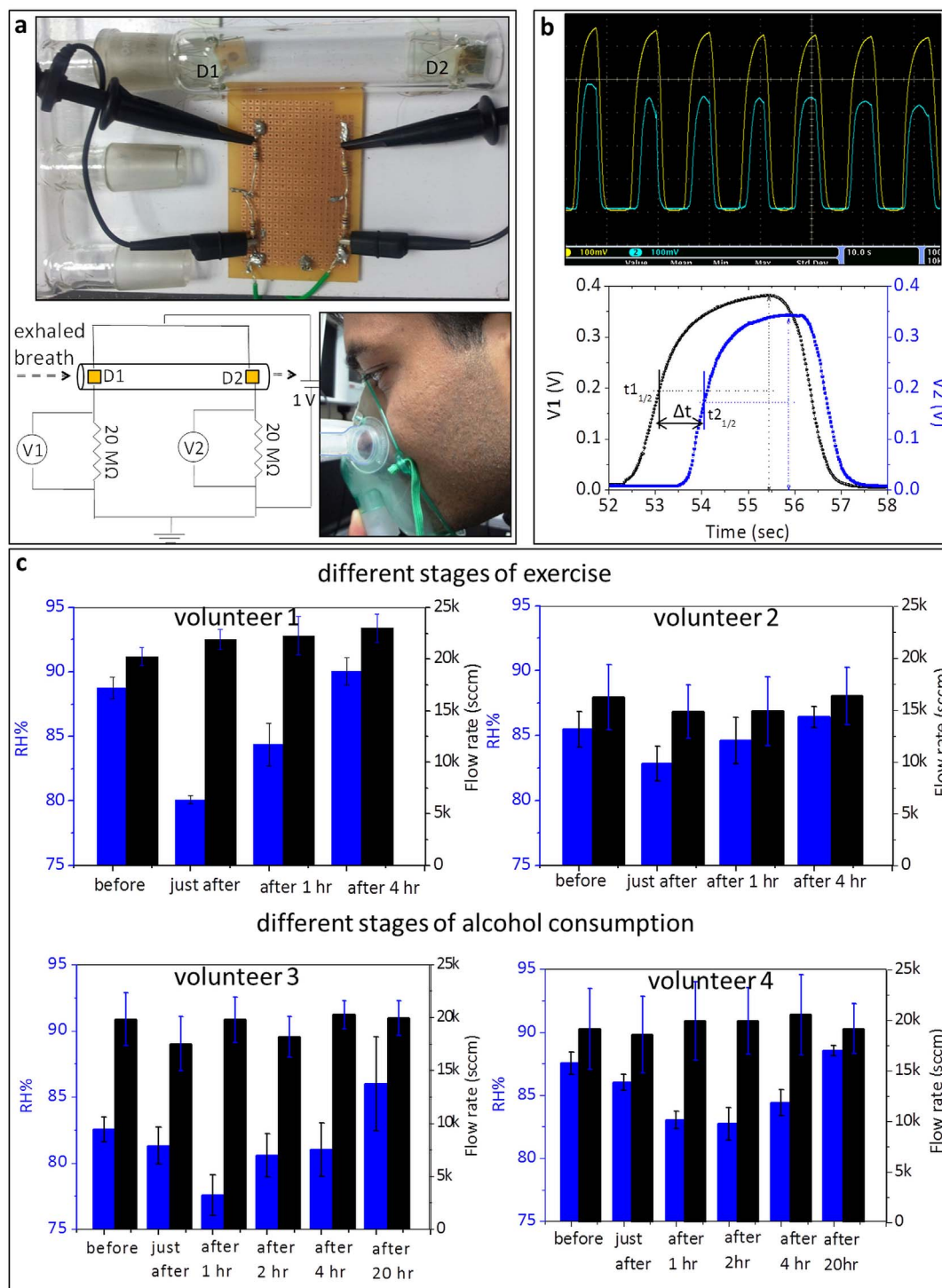


**Figure 8** | Integration of two humidity sensors for simultaneous measurement of humidity and flow of the exhaled human breath. (a) A photograph of the humidity cum flow sensor is shown in top. It has two supramolecular humidity sensors, D1 and D2, placed apart at a distance of 8 cm inside a glass tube of inner diameter 21 mm. The circuit diagram of the experimental set up is shown below (left). Two devices are connected in parallel and applied a bias of 1 V. Two resistors (20 MΩ each) are connected in series with the devices to give out voltage signals to an oscilloscope. A photograph of a volunteer performing breathing trial (below, right). A commercially available breathing mask was used to carry the exhaled breath over D1 and D2 sensors. After every breath out, the stray humidity in the glass tube was driven away by flushing with dry N<sub>2</sub> for a second while the volunteer inhaled. (b) Simultaneous humidity and flow sensing from the integrated device. The screen image of oscilloscope output of exhaled breath from a healthy individual (top). Below is a single breathing cycle showing calculation of 'Δt', the time difference between the two sensors to reach half of the peak value. (c) Demonstration of integrated device for human breath applications. Histogram plots showing variation of humidity and flow in the exhaled breath by exercise induced dehydration at different stages and by alcohol induced dehydration before and after alcohol consumption.



mouth<sup>34</sup>, as the former can be considered as a better representative of the lung hydration levels (with no interference from mouth saliva). The volunteer was made to breath comfortably but consistently such that the flow rate of breath was in a reasonably narrow range (20–30 kscm). The data shown in Fig. 8c were collected from four volunteers. Average RH and flow rate values obtained for volunteer 1 (male) in normal conditions were  $88.8 \pm 0.8\%$  and  $20.2 \pm 0.8$  kscm respectively (see histogram in Fig. 8c and Supplementary Fig. S7a). The volunteer was then made to run around 10 km in nearly 1 hr. After relaxing for few minutes, both the quantities were measured again (see histogram in Fig. 8c). It is interesting to see a sharp decline in the RH value in the exhaled breath after exercise ( $80.1 \pm 0.3\%$ ), which is understandable as the volunteer got dehydrated due to perspiration. The volunteer was indeed feeling thirsty, but was restrained from consuming food and water. When measurements were done after 1 hr, surprisingly, we found a gradual recovery of RH in the breath ( $84.4 \pm 1.6\%$ ). It appears that water from the internal body fluid was diverted towards the respiratory system which reflects in the breath RH level returning to normalcy ( $90.1 \pm 1.1\%$ , see histogram in Fig. 8c). Human lung tissue is known to maintain high degree of wetness for efficient exchange of gases and when dehydration occurs, it is susceptible to dry out thereby reducing the water content in the exhaled breath. However in our study, we have found that RH in the breath regained even under the dehydrated condition, clearly indicating that the lung tissue, by its nature, regenerated moisture on its (alveolar) surface from various metabolic processes. Upon water intake after the 1 hr measurement, the RH value completely regained (Fig. 8c). As shown on the right in Fig. 8c, a similar but mild trend was observed in the case of a female volunteer who undertook to run 3 km in nearly 30 minutes (see Fig. 8c and Supplementary Fig. S7b).

Another important situation of body dehydration relates to alcohol consumption<sup>57</sup>. Here, we examined the relative humidity in the exhaled breath to see the effect of alcohol consumption (but not as alcohol sensor). In the given two instances (Fig. 8c, bottom), the male volunteers 3 and 4 after consuming alcohol (beer, 8% alcohol, 2 L) were restrained from consuming food and water. We observed a decline in the RH following alcohol consumption due to dehydration in the body. However, the RH values recovered in spite of not feeding water (see bottom histograms in Fig. 8c and Supplementary Fig. S8). The variation in breath alcohol concentration (BAC) was monitored at every stage; RH declined with increased BAC (Supplementary Table S2). The situation is similar to that induced by physical exercise. Among many other control experiments, we have also monitored the RH of exhaled breath when a volunteer was made to drink plenty of plain water to cause excessive hydration; indeed, it was well reflected in the breath RH measurements (see Supplementary Fig. S9). Thus in this study, we have measured both flow and RH for every cycle where flow in narrow range ensures good sampling, removing other influences on RH. While this is a preliminary study of body dehydration monitored through RH in the breath, the study should open up new insights into diagnosis through breath analysis.

## Discussion

An ultra-fast, wide range, highly sensitive resistive humidity sensor has been developed based on a coronene-viologen derivative system, self-assembled in the form of nanofibre from water. While a film of nanofibres exhibited high sensitivity ( $\approx 10^4$ ), devices with few nanofibres showed extremely fast response ( $\approx 10$  ms). Using UV-vis, XRD and AFM measurements, we have found that the  $\pi$ - $\pi$  interaction between the donor and the acceptor molecules depends sensitively on the surrounding humidity influencing electrical conduction across the nanofibre. The fabricated devices were found to be stable over 8 months during the study. As is evident, these devices can be used in various contexts. The RH value close to a drop of water was determined by approaching it with a nanofibre film sensor. Fast

response devices made of few nanofibres have been effectively employed for dynamic monitoring of human breath. Using two such devices in a circuit, a flow cum humidity sensor has also been fabricated and its application has been demonstrated in analysing dehydrated conditions. As the sensing element is a simple organic system from solution processes, these devices are essentially of low cost and also environment friendly. Potential applications in personal health-care as use-and-dispose devices, is evident.

## Methods

**Synthesis of CS-DMV nanofibres.** The detailed procedure can be found in Reference<sup>43</sup>. In brief, CS (coronene tetracarboxylate) was synthesized by a twofold oxidative benzogenic Diels–Alder reaction of perylene with N-ethyl maleimide and subsequent hydrolysis with KOH in methanol. DMV (dodecyl methyl viologen) was synthesized from 4,4'-bipyridine by controlled reaction on one nitrogen with dodecyl bromide to give mono pyridinium ion and followed by treating the with methyl iodide to amphiphilic dicationic bipyridine (DMV). The charge-transfer fibres have been assembled from injection of a methanol solution of DMV, in which the viologens are molecularly dissolved, to the aqueous solution containing free CS molecules (10% v/v methanol in water).

**Characterisation.** The structural analysis was carried out by X-ray diffraction using Bruker D8 Discover diffractometer attached with temperature and humidity controlled stage. Cu K $\alpha$  ( $\lambda = 1.5419$  Å) was used as X-ray source. Atomic force microscopy (AFM) was performed using Multimode, Veeco digital instruments, USA with Nanoscope IV controller. The humidity control was achieved by using an environmental hood with flow of water vapors of different RH 15%, 42% and 62% continuously for 15 minutes. The images were collected in the tapping mode using Si cantilevers. The FE-SEM imaging was done using a Nova NanoSEM 600 (FEI Co., The Netherlands) by drop casting the aqueous solution on Si(100) substrate followed by drying in vacuum and was operated with an accelerating voltage of 10 kV. Absorption spectra were recorded on a Perkin Elmer Lambda 900 UV-VIS-NIR Spectrometer using 1 mm path length cuvette. To analyse the intensity variation with increasing RH, a baseline was drawn for each spectrum using Origin 8.0 software in the region of interest, 400 to 600 nm. The raw data was then subtracted from the baseline. Vapors of different RH were obtained by controlling the equilibrium vapor pressure of sulphuric acid<sup>15</sup>. A humidity cell was constructed for rapid switching of RH and switching between two RH levels was done using a Tee with flow rate of 200–300 sccm. A commercial humidity meter Testo 410-2 was used to measure the obtained RH. For alcohol monitoring a commercial alcohol meter (BAC<sup>TRACK</sup> B70) was used. We confirm that the Ethical Committee of the JNCASR approved all the experiments described in this paper. Further, informed consent was obtained from all the subjects.

**Device fabrication.** The glass substrates were cleaned in piranha solution followed by washing in distilled water several times. Metallic contacts were made by physical vapor deposition of Au by shadow masking using a resistive thermal evaporator (HindHivac, India) at a base pressure of  $10^{-6}$  Torr. A Keithley Semiconductor Characterization System 4200 was used to measure device characteristics. An Oscilloscope Tektronix DPO 4104 was used to measure the voltage drop across resistors.

1. Traversa, E. Ceramic sensors for humidity detection: the state-of-the-art and future developments. *Sens. Actuators, B* **23**, 135–156 (1995).
2. Wang, Y., Besant, R. W., Simonson, C. J. & Shang, W. Application of humidity sensors and an interactive device. *Sens. Actuators, B* **115**, 93–101 (2006).
3. Kebabian, P. L., Kolb, C. E. & Freedman, A. Spectroscopic water vapor sensor for rapid response measurements of humidity in the troposphere. *J. Geophys. Res., [Atmos.]* **107**, 4670 (2002).
4. Kuban, P., Berg, J. M. & Dasgupta, P. K. Durable microfabricated high speed humidity sensors. *Anal. Chem.* **76**, 2561–2567 (2004).
5. Laville, C. & Pellet, C. Comparison of three humidity sensors for a pulmonary function diagnosis microsystem. *IEEE Sens. J.* **2**, 96–101 (2002).
6. Laville, C. & Pellet, C. Interdigitated humidity sensors for a portable clinical microsystem. *IEEE Trans. Biomed. Eng.* **49**, 1162–1167 (2002).
7. Niesters, M. *et al.* Validation of a novel respiratory rate monitor based on exhaled humidity. *Br. J. Anaesth.* **109**, 981–989 (2012).
8. Chen, Z. & Lu, C. Humidity sensors: A review of materials and mechanisms. *Sensor Lett.* **3**, 274–295 (2005).
9. Kuang, Q., Lao, C., Wang, Z. L., Xie, Z. & Zheng, L. High sensitivity humidity sensor based on a single SnO<sub>2</sub> nanowire. *J. Am. Chem. Soc.* **129**, 6070–6071 (2007).
10. Cheng, B., Tian, B., Xie, C., Xiao, Y. & Lei, S. Highly sensitive humidity sensor based on amorphous Al<sub>2</sub>O<sub>3</sub> nanotubes. *J. Mater. Chem.* **21**, 1907–1912 (2012).
11. Yin, H. *et al.* Porous V<sub>2</sub>O<sub>5</sub> micro/nano-tubes: Synthesis via a CVD route, single-tube-based humidity sensor and improved Li-ion storage properties. *J. Mater. Chem.* **22**, 5013–5019 (2011).





12. Buvailo, A. I., Xing, Y., Hines, J., Dollahon, N. & Borguet, E. TiO<sub>2</sub>/LiCl based nanostructured thin film for humidity sensor applications. *ACS Appl. Mater. Interfaces* **3**, 528–533 (2011).
13. Li, Z. *et al.* Highly sensitive and stable humidity nanosensors based on LiCl doped TiO<sub>2</sub> electrospun nanofibers. *J. Am. Chem. Soc.* **130**, 5036–5037 (2008).
14. Steele, J. J., Taschuk, M. T. & Brett, M. J. Nanostructured metal oxide thin films for humidity sensors. *IEEE Sens. J.* **8**, 1422–1429 (2008).
15. Feng, J. *et al.* Giant moisture responsiveness of VS<sub>2</sub> ultrathin nanosheets for novel touchless positioning interface. *Adv. Mater.* **24**, 1969–1974 (2012).
16. Jiang, P. *et al.* Aluminium doped n-type ZnS nanowires as high-performance UV and humidity sensors. *J. Mater. Chem.* **22**, 6856–6861 (2012).
17. Borini, S. *et al.* Ultrafast graphene oxide humidity sensors. *ACS Nano* **7**, 11166–11173 (2013).
18. Alwis, L., Sun, T. & Grattan, K. T. V. Optical fibre-based sensor technology for humidity and moisture measurement: Review of recent progress. *Measurement* **46**, 4052–4074 (2013).
19. Yeo, T. L., Sun, T. & Grattan, K. T. V. Fibre-optic sensor technologies for humidity and moisture measurement. *Sens. Actuators, A* **144**, 280–295 (2008).
20. Mehrabani, S., Kwong, P., Gupta, M. & Armani, A. M. Hybrid microcavity humidity sensor. *Appl. Phys. Lett.* **102**, 241101–241104 (2013).
21. Steffens, C., Manzoli, A., Leite, F. L., Fatibello, O. & Herrmann, P. S. P. Atomic force microscope microcantilevers used as sensors for monitoring humidity. *Microelectron. Eng.* **113**, 80–85 (2014).
22. Sharma, A. K. & Gupta, A. Design of a plasmonic optical sensor probe for humidity-monitoring. *Sens. Actuators, B* **188**, 867–871 (2013).
23. Amin, E. M. & Karmakar, N. C. Development of a low cost printable chipless RFID humidity sensor. *IEEE Sens. J.* **14**, 1 (2014).
24. Mattana, G. *et al.* Woven temperature and humidity sensors on flexible plastic substrates for e-textile applications. *IEEE Sens. J.* **13**, 3901–3909 (2013).
25. Saeidi, N., Strutwolf, J., Marechal, A., Demosthenous, A. & Donaldson, N. A Capacitive humidity sensor suitable for CMOS integration. *IEEE Sens. J.* **13**, 4487–4495 (2013).
26. Kulwicki, B. M. Humidity sensors. *J. Am. Ceram. Soc.* **74**, 697–708 (1991).
27. Dimitrakopoulos, C. D. & Malenfant, P. R. L. Organic thin film transistors for large area electronics. *Adv. Mater.* **14**, 99–117 (2002).
28. Guo, Y., Yu, G. & Liu, Y. Functional organic field-effect transistors. *Adv. Mater.* **22**, 4427–4447 (2010).
29. Toniolo, R. & Hümmligen, I. A. Simple and fast organic device encapsulation using polyisobutene. *Macromol. Mat. Eng.* **289**, 311–314 (2004).
30. Hoeben, F. J. M., Jonkheijm, P., Meijer, E. W. & Schenning, A. P. H. J. About supramolecular assemblies of  $\pi$ -conjugated systems. *Chem. Rev.* **105**, 1491–1546 (2005).
31. Aida, T., Meijer, E. W. & Stupp, S. I. Functional supramolecular polymers. *Science* **335**, 813–817 (2012).
32. Fabiano, S. *et al.* Supramolecular order of solution processed peryleneimide thin films: High performance small-channel n-type organic transistors. *Adv. Funct. Mater.* **21**, 4479–4486 (2011).
33. Huang, Z. *et al.* Pulsating tubules from noncovalent macrocycles. *Science* **337**, 1521–1526 (2012).
34. Operamolla, A. & Farinola, G. M. Molecular and supramolecular architectures of organic semiconductors for field effect transistor devices and sensors: A synthetic chemical perspective. *Eur. J. Org. Chem.* **3**, 423–450 (2011).
35. Moulin, E., Cid, J.-J. & Giuseppone, N. Advances in supramolecular electronics – from randomly self-assembled nanostructures to addressable self-organized interconnects. *Adv. Mater.* **25**, 477–487 (2013).
36. Schenning, A. P. H. J. & Meijer, E. W. Supramolecular electronics; nanowires from self-assembled small  $\pi$ -conjugated systems. *Chem. Commun.* **26**, 3245–3258 (2005).
37. Herzer, N. *et al.* Printable optical sensors based on H-bonded supramolecular cholesteric liquid crystal networks. *J. Am. Chem. Soc.* **134**, 7608–7611 (2012).
38. Briseno, A. L., Mannsfeld, S. C. B., Jenekhe, S. A., Bao, Z. & Xia, Y. Introducing organic nanowire transistors. *Mater. Today* **11**, 38–47 (2008).
39. Zang, L., Che, Y. & Moore, J. S. One dimensional self-assembly of planar  $\pi$ -conjugated molecules: Adaptable building blocks for organic nanodevices. *Acc. Chem. Res.* **41**, 1596–1608 (2008).
40. Zhang, C., Yan, Y., Sheng Zhao, Y. & Yao, J. Synthesis and applications of organic nanorods, nanowires and nanotubes. *Ann. Rep. Prog. Chem. Sect. C* **109**, 211–239 (2013).
41. Min, S.-Y. *et al.* Large-scale organic nanowire lithography and electronics. *Nat. Commun.* **4**, 1773 (2013).
42. Sagade, A. A. *et al.* High mobility field effect transistors based on supramolecular charge transfer nanofibres. *Adv. Mater.* **25**, 559–564 (2013).
43. Rao, K. V., Jayaramulu, K., Maji, T. K. & George, S. J. Supramolecular hydrogels and high aspect ratio nanofibers through charge transfer induced alternate coassembly. *Angew. Chem. Int. Ed.* **49**, 4218–4222 (2010).
44. Sagade, A. A., Venkata Rao, K., George, S. J., Datta, A. & Kulkarni, G. U. A charge transfer single crystal field effect transistor operating at low voltages. *Chem. Commun.* **49**, 5847–5849 (2013).
45. Hakim, M. *et al.* Diagnosis of head-and-neck cancer from exhaled breath. *Br. J. Cancer* **104**, 1649–1655 (2011).
46. Kim, K. H., Jahan, S. A. & Kabir, E. A review of breath analysis for diagnosis of human health. *Trends Anal. Chem.* **33**, 1–8 (2012).
47. Peng, G. *et al.* Detection of lung, breast, colorectal, and prostate cancers from exhaled breath using a single array of nanosensors. *Br. J. Cancer* **103**, 542–551 (2010).
48. Peng, G. *et al.* Diagnosing lung cancer in exhaled breath using gold nanoparticles. *Nat. Nano.* **4**, 669–673 (2009).
49. Righettoni, M., Tricoli, A. & Pratsinis, S. E. Si:WO<sub>3</sub> sensors for highly selective detection of acetone for easy diagnosis of diabetes by breath analysis. *Anal. Chem.* **82**, 3581–3587 (2010).
50. Tisch, U. & Haick, H. Arrays of chemisensitive monolayer-capped metallic nanoparticles for diagnostic breath testing. *Rev. Chem. Eng.* **26**, 171 (2010).
51. Boshier, P. R. *et al.* On-line, real time monitoring of exhaled trace gases by SIFT-MS in the perioperative setting: a feasibility study. *Analyst* **136**, 3233–3237 (2011).
52. Smith, D. & Spanel, P. The challenge of breath analysis for clinical diagnosis and therapeutic monitoring. *Analyst* **132**, 390–396 (2007).
53. Armstrong, L. E. Hydration assessment techniques. *Nutr. Rev.* **63**, S40–S54 (2005).
54. Perrier, E. *et al.* Hydration biomarkers in free-living adults with different levels of habitual fluid consumption. *Br. J. Nutr.* **109**, 1678–1687 (2013).
55. Shirreffs, S. M. Markers of hydration status. *Eur. J. Clin. Nutr.* **57**, S6–S9 (2003).
56. Gupta, J. K., Lin, C.-H. & Chen, Q. Characterizing exhaled airflow from breathing and talking. *Indoor Air* **20**, 31–39 (2010).
57. Hobson, R. M. & Maughan, R. J. Hydration status and the diuretic action of a small dose of alcohol. *Alcohol Alcohol.* **45**, 366–373 (2010).

## Acknowledgments

The authors thank Prof. C.N.R. Rao for his constant encouragement. They thank Mr. K. Venkata Rao for synthesising the molecules used in the study. They are thankful to the volunteers for their participation in data collection. This research work is supported by Department of Science and Technology (DST), New Delhi, India. A.A.S. is thankful to DST for Nano-Postdoc Fellowship. U.M. thank CSIR, India for a research fellowship.

## Author contributions


G.U.K. and A.A.S. conceived the idea, U.M., A.A.S. and G.U.K. designed the experiments, U.M. and A.A.S. performed the experiments and U.M., A.A.S., S.J.G. and G.U.K. analysed the data and all authors wrote the manuscript.

## Additional information

**Supplementary information** accompanies this paper at <http://www.nature.com/scientificreports>

**Competing financial interests:** The authors declare no competing financial interests.

**How to cite this article:** Mogera, U., Sagade, A.A., George, S.J. & Kulkarni, G.U. Ultrafast response humidity sensor using supramolecular nanofibre and its application in monitoring breath humidity and flow. *Sci. Rep.* **4**, 4103; DOI:10.1038/srep04103 (2014).

 This work is licensed under a Creative Commons Attribution-NonCommercial-NoDerivs 3.0 Unported license. To view a copy of this license, visit <http://creativecommons.org/licenses/by-nc-nd/3.0>